Journal of
Materials Chemistry C

Materials for optical, magnetic and electronic devices

Accepted Manuscript

This article can be cited before page numbers have been issued, to do this please use: A. FLUCK, V. Giuso, C. Liu, C. Gourlaouen, C. Cebrián, F. Polo, H. Su, A. Jouaiti and M. Mauro, *J. Mater. Chem. C*, 2026, DOI: 10.1039/D6TC00899B.

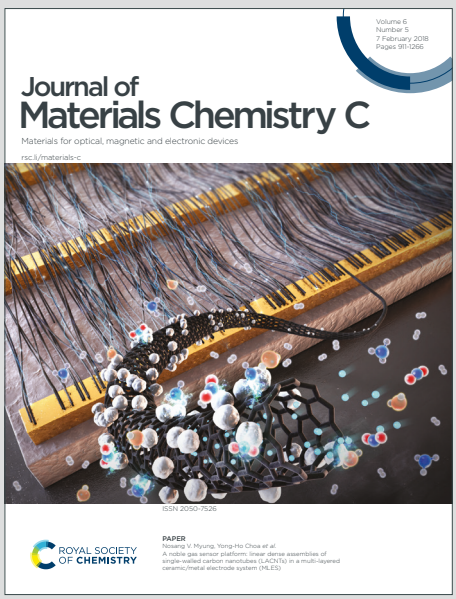

ROYAL SOCIETY OF CHEMISTRY

rsc.li/materials-c

View Article Online
DOI: 10.1039/D6TC00899B

Near Infrared Electroluminescence in Light-emitting Electrochemical Cells from Binuclear Copper(I) Complexes bearing π-extended Benzimidazole and Benzothiazole Ligands

Audrey Fluck,[a,†] Valerio Giuso,[b,†] Chun-Hsi Liu,[c,†] Christophe Gourlaouen,[d] Cristina Cebrián,[e] Federico Polo,[f,g] Hai-Ching Su,[c,*] Abdelaziz Jouaiti,[a,*] and Matteo Mauro,[b,e,*]

[a] *Laboratoire de Synthèse et Fonctions des Architectures Moléculaires, UMR7140 Chimie de la Matière Complexe, Université de Strasbourg & CNRS, 4 rue Blaise Pascal, 67000 Strasbourg (France). E-mail:* jouaiti@unistra.fr

[b] *Université de Strasbourg & CNRS, Institut de Physique et Chimie des Matériaux de Strasbourg UMR 7504, F-67034 Strasbourg, France*

[c] *Institute of Lighting and Energy Photonics, National Yang Ming Chiao Tung University, Tainan 71150, Taiwan. E-mail:* haichingsu@nycu.edu.tw

[d] *Laboratoire de Modélisation et Simulations Moléculaires, UMR 7140 Chimie de la Matière Complexe, Institut Le Bel, F-67081 Strasbourg, France*

[e] *Department of Chemical Sciences, University of Padova, Via Marzolo 1, 35121 Padova, Italy. E-mail*: matteo.mauro@unipd.it

[f] *Department of Molecular Sciences and Nanosystems, Ca' Foscari University of Venice, Via Torino 155, 30172 Venezia (Italy)*

[g] *European Centre for Living Technology (ECLT), Ca' Bottacin, 30124, Venice, Italy*

† These authors equally contributed to the work.

Abstract

The design of compounds that efficiently emits into the deep-red to near-infrared (NIR) region is still highly challenging, yet they can play pivotal role in optoelectronic devices for phototherapy, encryption and telecommunication technology. To date, examples of NIR-emissive earth-abundant Cu(I) complexes are still very rare in literature. Herein, a series of binuclear heteroleptic Cu(I) complexes, namely **Cu1**–**Cu4,** is presented and thoroughly characterized by means of chemical and (time-resolved) optical spectroscopies as well as single-crystal X-ray diffractometric analysis. The optical and electronic properties are further elucidated with the help of time-dependent density functional theory (TD-DFT) computations that confirms the nature of the transitions and excited states involved. It is shown that introduction of sulphur and nitrogen heteroatoms in the peripheral π-accepting coordinating

View Article Online
DOI: 10.1039/D6TC00899B

scaffolds, such as (substituted) benzimidazoles and benzothiazole, along with the thiazolo[5,4-*d*]thiazole bridging unit results in deep-red to NIR emissive complexes both in CH_2Cl_2 solution and in the solid state with long-lived emission with profile centred at λ_{em} = 734–776 nm and 644–757 nm, respectively, attributable to an emissive excited state with admixed ^{3}MLCT/^{3}LLCT character. Finally, derivative **Cu1** and **Cu4** are tested as electroluminescent materials in light-emitting electrochemical cells (LECs). The former displays deep-red electroluminescence (EL), λ_{EL} = 686–697 nm with external quantum efficiency (EQE) up to 0.5%; whereas the latter achieves NIR EL with λ_{EL} > 770 nm in combination with of high spectral stability, remarkably. Overall, the presented results demonstrate that Cu(I) complexes represents a valid alternative to precious metals for NIR EL devices.

Introduction

Near-infrared (NIR) light-emitting devices, including both inorganic and organic systems, have attracted significant attention owing to their promising applications in sensors, night-vision displays, biomedical devices, and optical telecommunications.[1] Among them, NIR organic light-emitting devices (OLEDs) offer several attractive advantages, such as low power consumption, compatibility with large-area fabrication, and mechanical flexibility. However, their practical implementation is still hindered by the requirement for complex multilayer device architectures and the instability of air-sensitive cathodes.

Solid-state light-emitting electrochemical cells (LECs)[2] provide a compelling alternative to conventional OLEDs by utilizing in situ electrochemical doping under electrical bias. The accumulation of mobile ions at the electrodes induces the formation of electrochemically doped layers, which effectively lower the carrier-injection barriers and promote balanced charge injection. As a result, LECs can employ air-stable metals as cathode materials, thereby reducing encapsulation requirements. Moreover, efficient electroluminescence (EL) can be achieved in a simple single-layer architecture that is readily compatible with solution-processing techniques.

NIR LECs[3] have been realized using a variety of emissive materials, including small molecules,[4–6] conjugated polymers,[7,8] ionic transition metal complexes (iTMCs),[9–12] and perovskites.[13] Among these systems, iTMC-based NIR LECs generally exhibit superior device efficiencies, primarily owing to the phosphorescent nature of iTMC emitters, which enables efficient exciton harvesting. However, many reported NIR iTMCs rely on rare transition

View Article Online
DOI: 10.1039/D6TC00899B

metals, such as ruthenium,[14,15] iridium,[16–19] osmium,[20] and platinum,[21] whose high cost significantly limits their prospects for large-scale applications. Consequently, increasing research efforts have been devoted to developing NIR iTMC emitters incorporating earth-abundant transition metals as more sustainable alternatives. Among the emerging candidates, copper(I) complexes have attracted particular interest as promising emitters for LECs due to the earth-abundant nature and low cost of copper. In addition, appropriately designed Cu(I) complexes can exhibit efficient excited-state processes, such as metal-to-ligand charge-transfer (MLCT) emission or thermally activated delayed fluorescence (TADF), enabling effective exciton utilization in EL devices. These features make Cu-based complexes attractive alternatives to rare-metal iTMCs for developing cost-effective NIR LECs.

Transition metal complexes (TMCs) that display NIR EL are still very limited in the literature and only rare examples deal with more abundant metals such as Cu(I) and Ag(I).[22–24] These complexes are particularly interesting because their d^{10} electronic configuration rules out the possibility of thermally accessible low-lying metal centered (MC) states that that would quickly deactivate non-radiatively.[25] The scarcity of described examples is mainly due to the three following reasons: *i*) smaller SOC constant possessed by the lighter metals compared to those lying on the second and third row (*e.g.* Pt(II), Ir(III)) (ζ_{Cu} = 857 cm^{-1}; ζ_{Ir} = 3909 cm^{-1}; ζ_{Pt} = 4481 cm^{-1}) yields complexes featured by reduces the singlet-triplet mixing (S–T) and slower radiative rate constant (k_r); *ii*) smaller energy gap between ground and excited state (S_0–T_1) increases the non-radiative vibronic coupling, thus increasing the k_{nr} (*energy gap law*); and, finally, red to NIR emitters possess intrinsically smaller k_r due to the third-power dependency with emission energy, as by Einstein's theory of spontaneous emission[26,27].

A notable class of luminescent Cu(I) coordination compounds is represented by cationic $[Cu^{I}(N^N)(P^P)]^+$ complexes, where N^N is a neutral polypyridyl bidentate ligand and P^P is a rigid bidentate diphosphine. The photophysical behaviour of these species, firstly investigated in the early 2000s by McMillin, Walton, *et al.*, is highly dependent on the geometry and nature of the ligands, as well as environmental parameters. Their emission typically arises from a triplet-manifold metal-to-ligand charge transfer excited states (^{3}MLCT) which formally entail an oxidation of the metal center to d^9 Cu(II) and preferentially adopt an equilibrium geometry closer to a square pyramidal arrangement owing to the large pseudo Jahn-Teller distortion effects. This leads to more efficient vibronic quenching of the lowest lying excited states (T_1–S_0) and exposes the metal to solvent-assisted exciplex deactivation processes. Employing a bulky, bidentate diphosphine prevents solvent quenching, and the P^P bridge can slightly alter

View Article Online
DOI: 10.1039/D6TC00899B

the energy of the d^{10} orbitals, thus modifying the MLCT energy gap and allowing for some degree of tuning in the emission through the diphosphine. Nevertheless, the largest influence on the emission profile is exerted by the N^N ligand, allowing $[Cu^{I}(N^N)(P^P)]^{+}$ complexes to be tuned to yield emission ranging from the blue-green to the red-NIR region of the visible spectrum.[28,29]

An exploit that has been found to bathochromically shift the emission profile is the introduction of sulphur heteroatoms in the N^N ligand, as their higher electron-accepting character and lower oxidation potential, reflected by their generally lower HOMO and LUMO energies, causes an overall decrease in the band gaps of transitions involving the π* MOs, leading to significantly longer emission wavelengths. This approach recently allowed to push the emission of Cu(I) in the NIR by employing simple pyridyl-benzothiazole ligands, obtaining complexes with emission in the range λ_{em} = 520–760 nm and PLQY values up to 10% in thin-film and powder form, but still barely detectable in CH_2Cl_2 solution, as described by Steffen *et al.*.[30] Costa *et al.* showed that employing more rigid diphosphines, such as Xantphos, enabled the preparation of Cu(I) and Ag(I) complexes which displayed red luminescence in the solid state and in proof-of-concept light-emitting devices with λ_{el} = 670 and 645 nm respectively, but external quantum efficiency (EQE) values not higher than *ca*. 0.01%.[22,31] A bathochromic shift of the emission can also be induced by dinuclearization of the complex having general formula $[Cu^{I}(P^P)(N^N–N^N)Cu^{I}(P^P)]^{2+}$, *e.g.* by employing a *bis*-bidentate 2,5-dipyridyl-thiazolo[5,4-*d*]thiazole bridging ligand. This approach has been successfully employed by our research group to prepare a new family of electroactive binuclear thiazolo[5,4-*d*]thiazole (TzTz) Cu(I) complexes that displayed λ_{EL} up to 780 nm in LECs, effectively being the first reported examples of a Cu(I)-based NIR device,[23] and later setting a record for the most bathochromically shifted emission of a Cu(I) LEC[24]. Herein, we explore the effect of introduction of π-accepting benzothiazole and benzimidazole scaffolds to achieve more stable NIR EL with binuclear Cu(I) complexes. These heteroatomic scaffold have been chosen for stabilizing the π* orbitals localized onto the coordinated bridging ligands in order to maintain longer wavelength emission, while potentially improving charge transport properties compared to previously investigated counterparts (Scheme 1).

View Article Online
DOI: 10.1039/D6TC00899B

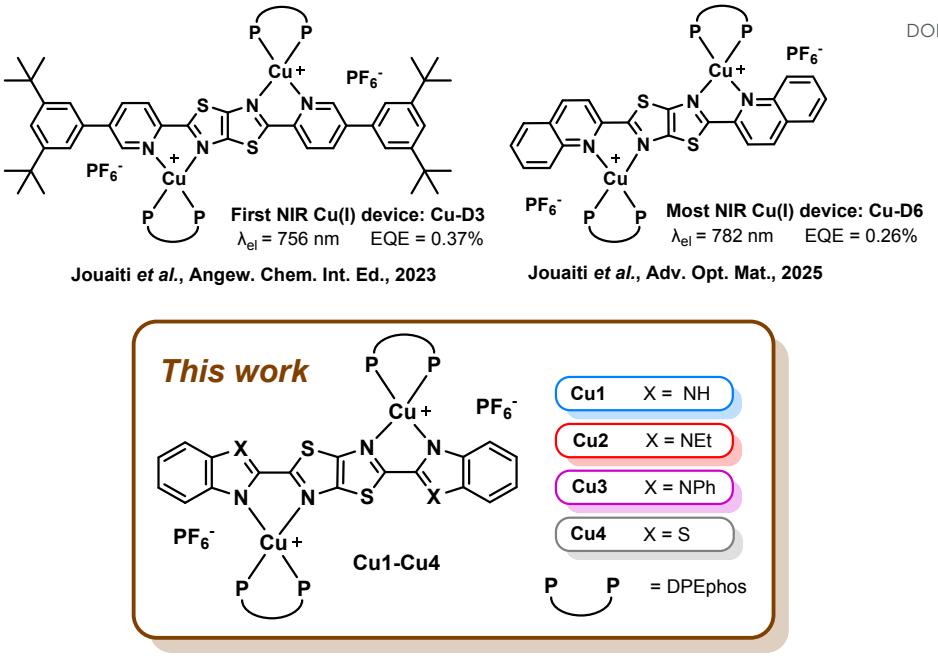

Scheme 1. Molecular structures of the two landmark Cu(I) NIR emitters previously published by our group (*top*) and of the new compounds **Cu1**–**Cu4** investigated this work (*bottom*).

Results and Discussion

Synthesis and X-ray structures

The selected ligands feature a π-extended thiazolo[5,4-*d*]thiazole (TzTz) core and two lateral 1-R-1*H*-benzo[*d*]imidazol-2-yl (R = H, Et and Ph for **L1**, **L2** and **L3**, respectively) and benzo[*d*]thiazol-2-yl (**L4**) moieties acting as the bridging *bis*-bidentate (N^N–N^N) scaffold. The schematic synthetic pathway employed for their synthesis is depicted in Scheme S1 of the Supporting Information alongside the corresponding ^{1}H, ^{13}C{^{1}H}, ^{31}P{^{1}H} NMR and high-resolution mass spectrometry (Figures S1–S19 of the Supporting Information). For the ligands, the procedure followed a straightforward condensation reaction between dithiooxamide and the corresponding aryl-carboxaldehyde in refluxing DMF yielding the desired product as pure powder after washing.[32,33]

Single crystals suitable for X-ray diffractometric analysis were obtained for **L3** and the ORTEP diagram is displayed in Figure S20 of the ESI (see Table S1 for the crystallographic refinement parameters). Ligand **L2** was prepared starting from the **L1** parental ligand via *N*-alkylation of the benzimidazolyl N-H group with iodoethane in hot DMF (Scheme S1). The synthesis of the binuclear Cu(I) complexes followed a one-pot two-step procedure (Scheme S2), where to a

solution of DPEphos (2 equiv.) in CH_2Cl_2 kept at room temperature was subsequently added the *tetrakis*-acetonitrile copper(I) precursor (2 equiv.) as PF_6^- salt, and the chromophoric ligand **L1**–**L4** (1 equiv.), yielding the target complex of general formula [Cu(P^P)(**L1**–**L4**)(P^P)]$(PF_6)_2$ (**Cu1**–**Cu4**, respectively), as a red solid in excellent yield (>90%) (see Scheme 1 for chemical structure). For the complexes, the $^{31}P\{^1H\}$ spectra displayed one single resonance in the region at δ *ca.* –12.0 ppm associated to the chelating phosphine that indicates that one single species is present in CD_2Cl_2 solution. Despite the somewhat labile nature of these binuclear species in solution, enhanced by the high electron-deficient nature of the ligands, all complexes yielded crystals suitable for X-ray crystallographic analysis by vapor diffusion of Et_2O in a CH_2Cl_2 solution of the complex. The crystal structure and packing of all the complexes was established by means of single crystal X-ray diffractometric analysis, which also confirmed the binuclear nature of all the species with general formula [Cu_2(**L1**–**4**)$(DPEphos)_2]^{2+}$ (see Figure 1 and S21-S22 of the ESI). The corresponding data can be found in Tables S2–S5 of the Supporting Information. Some relevant geometric parameters for **Cu1**–**Cu4** are indicated in Table 1, along with those of the reference complex **Cu-D3**[23] displayed in Scheme 1. Also, capped-sticks representation of the XRD structure of derivative **Cu-D3** is represented in Figure 2.

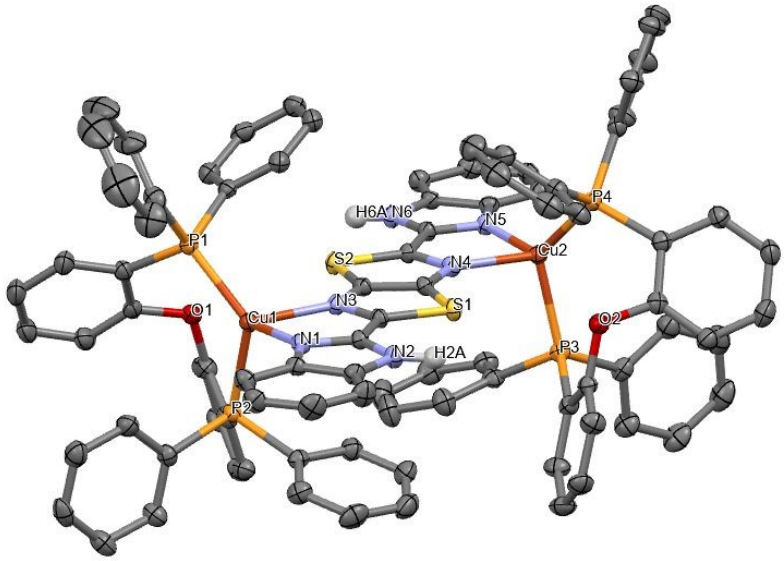

Figure 1. ORTEP diagram of **Cu1** shown at 50% probability. Hydrogen atoms (except the NH of the benzimidazole), solvent molecules and the PF_6^- counter anions are omitted for clarity.

Each Cu(I) ion adopts a distorted tetrahedral coordination geometry involving the chelating DPEphos (P^P) ligand and two nitrogen atoms of the 2,5-di(heteroaryl)thiazolo[5,4-*d*]thiazole (**L1**–**L4**). The bond lengths and angles relative to the tetrahedral Cu(I) centers are shorter than

View Article Online
DOI: 10.1039/D0TC00899B

those reported for similar mononuclear Ag(I) complexes, expectedly,[22,34–36] and comparable to those observed in similar Cu(I) complexes[23,24,30,37]. A selected list of geometrical parameters is summarized in Table 1. In compounds **Cu1** and **Cu4**, each DPEphos employs one of its phenyl rings in weak intramolecular π–π stacking on the imidazole (d = 3.46–3.61 Å), while another phenyl is involved in a S–π interaction with the central TzTz core (d = 3.28–3.53 Å) (see Figure 2a and 2d). Complex **Cu2** does not display any noticeable intramolecular interaction (Figure 2b) but a network of intermolecular π–π stacking interactions (d = 3.34 Å) is present at the supramolecular scale involving the 1-ethyl-1*H*-benzo[*d*]imidazol-2-yl moiety of the coordinated ligand **L2** of each neighbor complex. Complex **Cu3** displays some intramolecular π-π stacking between the phenyls of DPEphos, and two intramolecular C–H···π interaction between one of the phenyls of each phosphine and the adjacent phenyl substituent of the 1-phenyl-1*H*-benzo[*d*]imidazol-2-yl moiety (d = 3.186 Å) (Figure 2c).

Table 1. Selected bond lengths [Å] and angles [°] around one metal center for Cu(I) complexes **Cu1**–**Cu4** with their tetrahedral geometric indexes τ_4[38] and τ_4'[39]. N_{az} = nitrogen of the thiazolo[4,5-*d*]thiazole moiety, N_{py} = nitrogen of the peripheral moiety.

	M(1)–N_{az}	M(1)–N_{py}	M(1)–P(1)	M(1)–P(2)	$\tau_{4,M(1)}$	$\tau'_{4,M(1)}$
Cu-D3 [a]	2.063(3)	2.096(3)	2.2419(11)	2.2403(10)	0.87	0.86
Cu1	2.014(2)	2.136(2)	2.2201(7)	2.2392(6)	0.84	0.80
Cu2	2.018(3)	2.195(3)	2.2170(11)	2.2520(12)	0.85	0.82
Cu3	2.050(2)	2.131(2)	2.2137(7)	2.2788(7)	0.76	0.73
Cu4	2.099(5)	2.119(5)	2.2121(19)	2.2617(19)	0.77	0.75

[a] data corresponding to reference Cu(I) complex **Cu-D3** are taken from Ref. #[24].

While the dihedral distortion between the TzTz core and the peripheral substituents is not as marked as in the *bis*-(*t*-butylphenyl)-functionalized complex **Cu-D3** (Figure 2e), the TzTz ligands in **Cu1**–**Cu4** are not always planar. If we look at complex **Cu3** from the side (Figure 2c), we can see how the two peripheral benzimidazoles are oriented out of plane, likely due to the steric hindrance of the lateral N–Ph substituent. This can be observed, to a very small extent, on the N–Et derivative **Cu2** as well (Figure 2b). The τ_4 and τ'_4 values for these complexes are shown in Table 1 and reflect the considerations above. For complexes **Cu1** and **Cu2**, tetrahedral geometrical indexes are in the range 0.80–0.85 and indicate a minor distortion from the ideal T_d symmetry. Whereas, for derivatives **Cu3** and **Cu4** that bear bulkier benzothiazole- and *N*-phenyl benzimidazole these values decrease to 0.73–0.77, highlighting a slightly more significant distortion compared to their congeners, and approaching that of Ag(I) complexes[22].

View Article Online
DOI: 10.1039/D6TC00899B

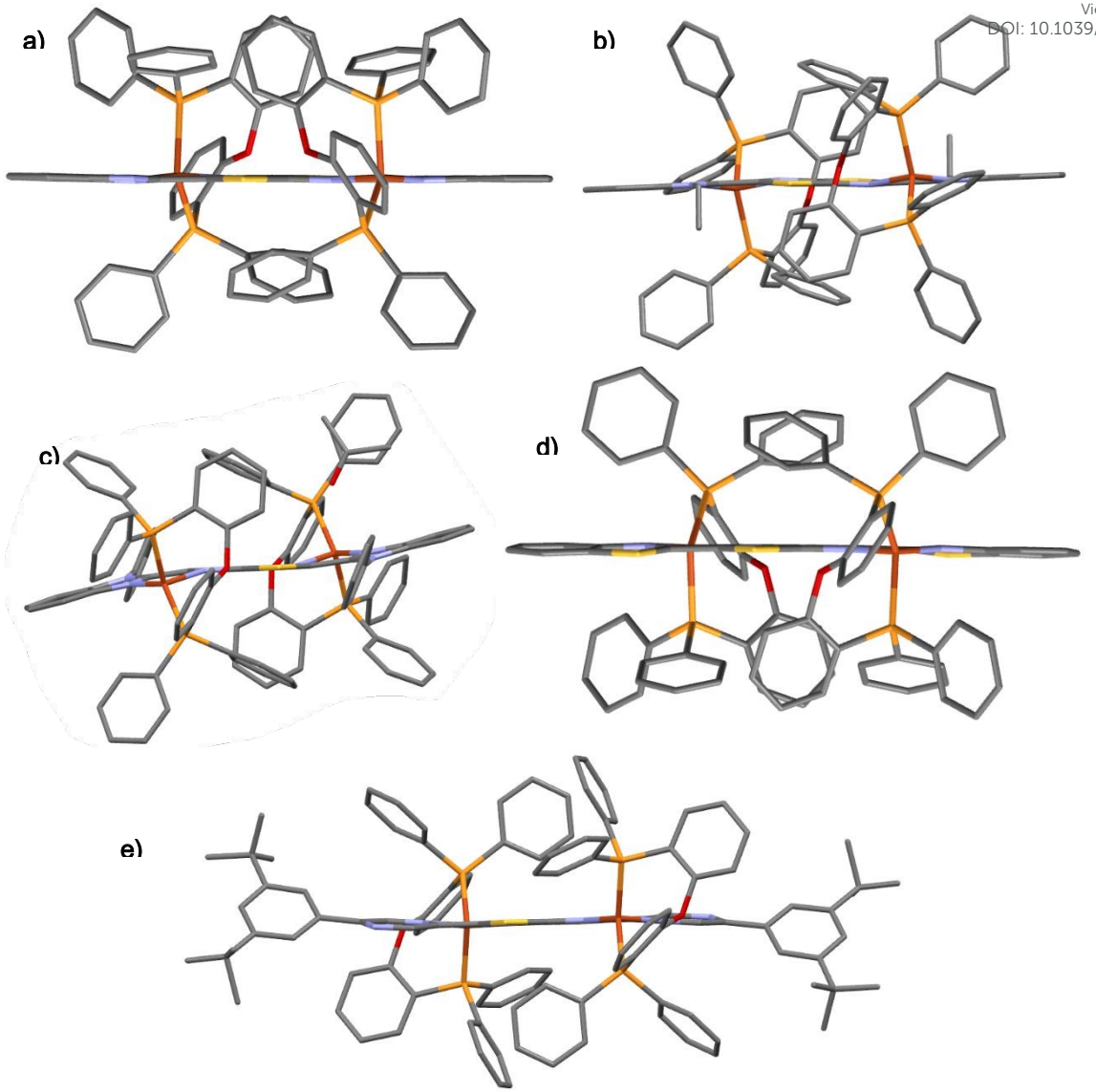

Figure 2. Capped sticks XRD structures viewed from the side of complexes **Cu1** (a), **Cu2** (b), **Cu3** (c), **Cu4** (d), and (e) reference complex **Cu-D3**[24]. Hydrogen atoms except the NH of the benzimidazole, solvent molecules and the PF_6^- counter anions are omitted for clarity.

Photophysical investigation

For the sake of comparison, the electronic absorption and emission spectra in dilute (3×10^{-6} M) air equilibrated CH_2Cl_2 for the four ligands **L1**–**L4** were acquired (Figure 3a and Table 2). A full photophysical characterization of these compounds was carried out and the results are in nice agreement with similar data recently reported by us for pyridyl- and quinolyl-functionalized TzTz ligands.[23,24,40] All the data, including measurements in the solid state and

View Article Online
DOI: 10.1039/D6TC00899B

in 77 K CH_2Cl_2 glassy matrix, can be found in the Supporting Information (Figures S23–S24 and Table S6).

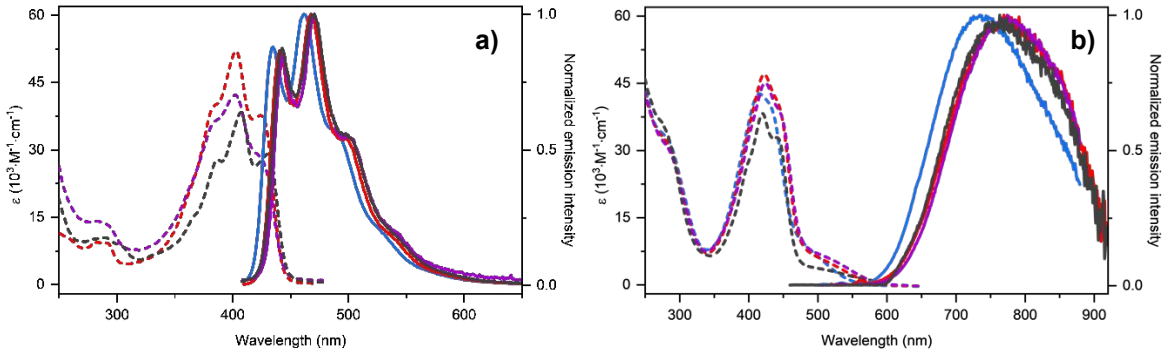

Figure 3. a) Electronic absorption (dashed traces) and emission spectra (solid traces) of ligands **L1** (blue), **L2** (red), **L3** (violet), and **L4** (grey) in dilute (3×10^{-6} M) air-equilibrated CH_2Cl_2 at room temperature upon excitation at λ_{exc} = 360 nm. b) Electronic absorption (dashed traces) and emission spectra (solid traces) of complexes **Cu1** (blue), **Cu2** (red), **Cu3** (violet), and **Cu4** (grey) in dilute (2×10^{-5} M) air-equilibrated CH_2Cl_2 at room temperature upon excitation at λ_{exc} = 460 nm.

Table 2. Electronic absorption and photoluminescence data in dilute air-equilibrated CH_2Cl_2 solution for ligands **L1**–**4**.

	λ_{max}, Abs(ε) [nm, (10^3 $M^{-1}cm^{-1}$]	λ_{em} [nm]	PLQY (%)	τ_{obs} [μs]	k_r [10^8 s^{-1}]	k_{nr} [10^8 s^{-1}]
L1	*poorly soluble*					
L2	282 (9.32), 292 (9.12), 382*sh* (38.98), 403 (51.95), 425 (37.57)	442, 468, 499*sh*, 543*sh*	64	1.21 ns	5.27	2.97
L3	284 (14.01), 293*sh* (12.99), 383*sh* (35.83), 402 (42.16), 426*sh* (27.64)	443, 470, 503*sh*, 542*sh*	39	1.25 ns	3.12	4.88
L4	290 (10.34), 305*sh* (8.45), 365*sh* (14.52), 387 (27.71), 407 (38.28), 431 (28.94)	444, 471, 504*sh*	9	0.41 ns	2.21	22.4

sh denotes a shoulder.

The electronic absorption spectra for **L1**–**L4** display, for all ligands, a weak band (ε = 0.1–1.4×10^4 M^{-1} cm^{-1}) at higher energies (λ_{abs} = 280–290 nm) that can be attributed to transitions with π–π* singlet-manifold locally excited (^{1}LE) character admixed with intramolecular charge transfer (^{1}ICT) processes from the central TzTz moiety towards the peripheral substituents. At lower energies, a much more intense (ε = 0.4–5.1×10^4 M^{-1} cm^{-1}) and structured band is observable at λ_{abs} = 380–430 nm and is mainly attributable to the ^{1}π–π* LE transitions localized onto the π-extended chromophoric thiazolo[5,4-*d*]thiazole scaffold. Upon coordination, these bands experience an expected bathochromic shift and intensity enhancement, reflecting the enlargement of the system and their admixing with ^{1}MLCT (^{1}dπ(Cu)→π_{TzTz}*) transitions and

further perturbation of the ligand-centered ^{1}LC ($^1\pi_{Ph}\rightarrow\pi_{BzIm}^*$) and ^{1}LLCT ($^1\pi_P\rightarrow\pi_{TzTz}^*$) transitions.

As for as complexes **Cu1**–**Cu4** are concerned, their photophysical behavior was firstly investigated in dilute (2×10^{-5} M) CH_2Cl_2 solution. The absorption and emission spectra are displayed in Figure 3b, and the photophysical data are summarized in Table 3. It is important to note that all four complexes are labile in highly diluted CH_2Cl_2 solutions, in particular upon repeated exposure to UV light. This can be noticed by the appearance of blue emission compatible with that of the ligands, and while dilute samples of **Cu1**-**Cu3** remained stable during their photophysical study, extended irradiation of **Cu4** led to enhanced degradation compared to its congeners. Regardless, even in the absence of light, dilute solutions of these complexes (10^{-5} M) cannot be stored for more than a day, and all photophysical studies were carried out on fresh samples.

For all complexes the electronic absorption spectra display an intense shoulder (ε = 3.1–3.3×10^4 M^{-1} cm^{-1}) at higher energies (λ_{abs} = 280–350 nm) attributed to ^{1}LLCT $^1\pi_{Ph}\rightarrow\pi_{BzIm}^*$ transitions involving the aromatic groups of the phosphine ligands and the benzimidazole (bim) and benzothiazole (btz) substituents. At lower energies, an intense (ε = 3.7–6.5×10^4 M^{-1} cm^{-1}) and structured band is observable at λ_{abs} = 380–450 nm and is mainly attributable to admixed ^{1}LC/^{1}MLCT transitions involving the π-extended TzTz ligand and Cu(I). The absorption shoulders at even lower energy, located at λ_{abs} = 475–550 nm, are much broader and less intense (ε = 0.3–0.7×10^4 M^{-1} cm^{-1}) and can be ascribed to a mixed transition with singlet-manifold metal-to-ligand charge transfer (^{1}MLCT) and ligand-to-ligand charge transfer (^{1}LLCT) with ^{1}dπ(Cu)$\rightarrow\pi_{TzTz}^*$ and $^1\pi_P\rightarrow\pi_{TzTz}^*$ character, respectively. Overall, the absorption profiles of the four complexes moderately reflect the increasing π-accepting ability of the substituted TzTz cores, along the series btz (**Cu4**) → bim (**Cu1**) → Et-bim (**Cu2**) → Ph-bim (**Cu3**), with their $\lambda_{abs,max}$ being 416, 420, 423 and 424 nm respectively.

Table 3. Electronic absorption and photoluminescence data in dilute degassed and air-equilibrated CH_2Cl_2 solution for complexes **Cu1**–**Cu4**.

	λ_{max}, Abs(ε) [nm, (10^3 M^{-1}cm^{-1}]	λ_{em} [nm]		PLQY (%)		τ_{obs} [μs]	τ_{ave} [μs]	τ_{obs} [μs]	τ_{ave} [μs]	k_r [10^5 s^{-1}]	k_{nr} [10^5 s^{-1}]
	air	air	deg	air	deg	air		deg			
Cu1	282*sh* (32.82), 420 (42.68), 433 (40.21), 495*sh* (7.66)	734	734	0.38	0.54	0.316		0.401 (98%) 10.29 (2%)	3.36	1.61	28.1
Cu2	282*sh* (31.55), 423 (46.75), 444*sh* (41.18), 517*sh* (5.66)	776	734	0.21	0.55	0.110 (97%)	0.198	0.128 (90%)	9.72	0.57	9.72

View Article Online
DOI: 10.1039/D6TC00899B

						0.672 (3%)		10.73 (10%)			
Cu3	282*sh* (30.95), 424 (45.68), 447*sh* (40.09), 515*sh* (6.90)	775	746	0.24	0.45	0.123 (99%) 0.729 (1%)	0.152	0.125 (97%) 14.30 (3%)	11.2	0.40	8.56
Cu4	274 (33.51), 281*sh* (32.06), 396*sh* (26.11), 416 (38.67), 441 (32.91), 506*sh* (3.08)	764	764	0.09	0.14	0.336		0.549 (99%) 11.7 (1%)	0.973	1.44	101

sh denotes a shoulder.

Upon excitation in the lower-lying ^{1}MLCT band (λ_{exc} = 440–480 nm), the four complexes display photoluminescence in dilute degassed and air-equilibrated CH_2Cl_2 with its maximum into the deep-red to NIR region of the electromagnetic spectrum arising from an excited state with admixed ^{3}MLCT/^{3}LLCT character. (Figure 3b and Table 3). The broad and featureless emission profile (FWHM ≈ 3400 cm^{-1}, ≈ 210 nm) presents a $\lambda_{em,max}$ in the range 734–775 nm, with complexes **Cu2**–**Cu3** being the most bathochromically shifted. Adopting the more conservative CIE 17-21-004[41] lower boundaries for NIR (> 780 nm), half of the emission of the complexes in dilute CH_2Cl_2 falls in the NIR, with %NIR values of *ca*. 48–51%. As expected from the energy gap law, the bathochromic shift in the emission is accompanied by a lowering of the photoluminescence quantum yield (PLQY) and a shortening of the excited state lifetime, and these effects can be seen particularly well by comparing the photophysical properties of complexes **Cu1** and **Cu4** in dilute degassed CH_2Cl_2 solution, which show $\lambda_{em,max}$, PLQY and $\tau_{avg,deg}$ of 734 nm, 0.54%, 3.36 μs and 764 nm, 0.14% and 0.973 μs respectively. This effect, caused by the increased vibronic coupling between the T_1 and S_0 state, is reflected by the estimated radiative (k_r) and non-radiative (k_{nr}) rate constants characterizing the emissive excited state (Table 3). These constants have been calculated by using the following equations (eqns. 1–2):

$$k_r = \frac{PLQY}{\tau} \quad \text{(eqn. 1)}$$

$$k_{nr} = \frac{1-PLQY}{\tau} \quad \text{(eqn. 2)}$$

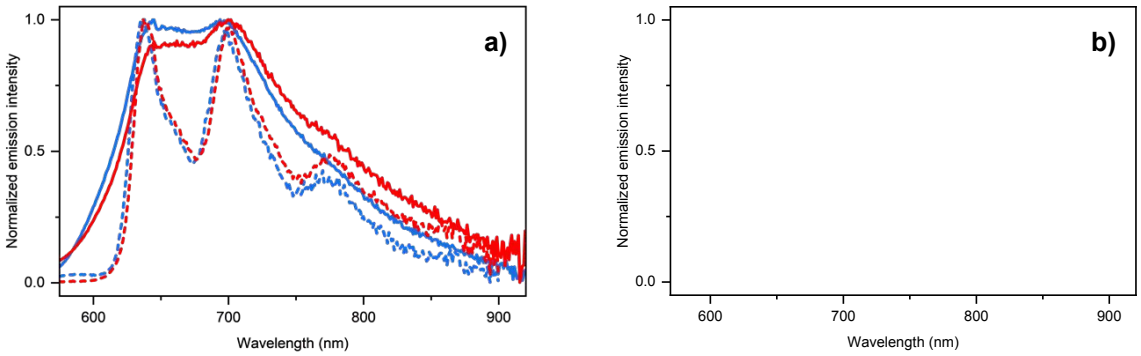

View Article Online
DOI: 10.1039/D6TC00899B

Figure 4. Emission spectra of a) complexes **Cu1** (blue), **Cu2** (red), and b) complexes **Cu3** (violet) and **Cu4** (grey) as neat powders under vacuum at 298 K (solid traces) and in CH_2Cl_2 glassy matrix at 77 K (dashed traces). Spectra were recorded upon excitation at λ_{exc} = 450 and 480 nm respectively.

Table 4. Photophysical data recorded for complexes **Cu1**–**4**as neat powders under vacuum and in CH_2Cl_2 glassy matrix at 77 K.

cmpd	λ_{em} [nm]		PLQY (%)	τ_{ave} [µs]		k_r [10^3 s^{-1}]	k_{nr} [10^3 s^{-1}]
	powder	77 K (CH_2Cl_2)	powder	powder	77 K (CH_2Cl_2)	powder	
Cu1	644, 696	638, 697, 770	4	67.2	293	0.59	14.3
Cu2	644, 700	638, 700, 775	2	70.9	499	0.28	13.8
Cu3	650, 715	647, 712, 788	2	72.9	211	0.27	13.4
Cu4	757	682, 751, 834	1	0.89	71.9	11.2	1106

sh denotes a shoulder.

Photophysical data of **Cu1**–**Cu4** in the solid state as neat powders and in CH_2Cl_2 glassy matrix at 77 K are summarized in Table 4 and the emission spectra shown in Figure 4. Upon lowering the temperature down to 77 K, CH_2Cl_2 samples of complexes **Cu1**–**Cu4** display a more structured emission profile with a clear vibronic progression that is hypsochromically shifted by *ca.* 1570–2050 cm^{-1} indicating a small rigidochromic effect due to the limited charge transfer nature of the emitting excited state at lower temperature. This spectral shift is accompanied by a substantial increase of the excited state lifetime up to τ_{avg} = 72–500 µs. These observations agree with the large triplet nature of the emissive excited state that can be with confidence described as largely ^{3}LC in nature. In addition, the observed large hypsochromic shift observed for glassy matrix samples compared to room temperature ones might allow us to rule out thermally-activated delayed fluorescence (TADF) processes.[42]

In powder form the complexes show broad and somewhat structured emission which is not noticeably affected by the presence of the quenching species dioxygen, but its removal causes a *ca*. 1% increase in the PLQY and a *ca.* 10% prolongation of the excited-state lifetimes. For this reason, measures on powder samples were carried out in quartz tubes held under dynamic vacuum (*ca.* 10 mbar), revealing PLQY values as high as 4% for **Cu1** and lifetimes in the range of 67–73 µs for complexes **Cu1**–**Cu3**. Complex **Cu4**, the most NIR of the series, displays the lowest PLQY (1%) and lifetime (0.89 µs), in agreement with the energy gap law. It should be noted that while these results may be low compared to other orange-red photoactive TMCs based on Ir(III) and Pt(II) complexes,[43–45] the lower energy of their NIR emission makes these

View Article Online
DOI: 10.1039/D6TC00899B

performances comparable to those of the landmark complexes we recently published (Scheme 1).[23,24]

Computational investigation

To further elucidate the photophysical behaviour of this family of NIR emitters, ground state geometries, absorption spectra and optimized excited states of both singlet and triplet manifolds have been computed by means of (time-dependent) density functional theory (TD-)DFT calculations.

Experimental and computed structures (Table S7) are in good agreement, both displaying a distorted tetrahedral geometry at the Cu centers with a slight lengthening of one of the Cu-N_{TzTz} distances. Upon geometry optimization of **Cu2** and **Cu3**, a pyramidal distortion around the $[Cu(N^N)(P^P)]^+$ tetrahedron occurs yielding the formation of a π-stacking interaction between one of its phenyl rings of the P^P chelates and one of the two benzimidazole fragments, in a similar fashion to what observed experimentally in the X-ray structure of derivatives **Cu1** and **Cu4** (*cf.* Figure S25 *vs* Figures 1 and 2).

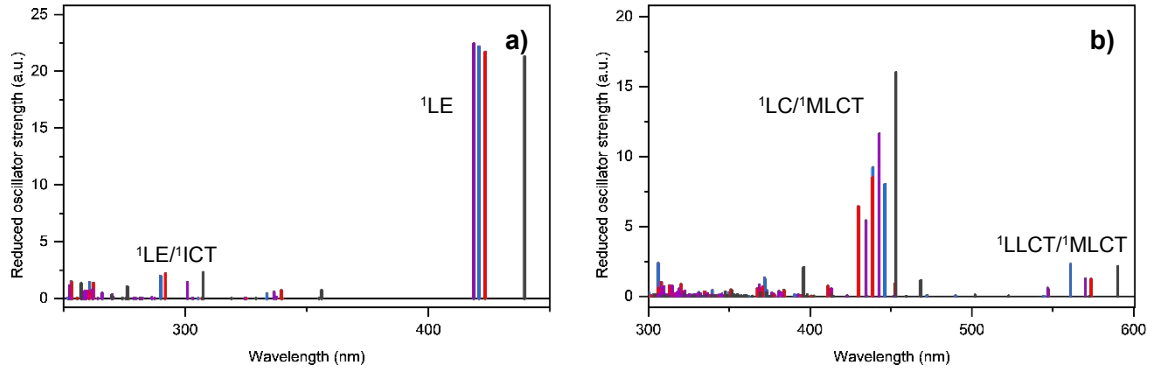

Figure 5. Electronic absorption transitions computed in CH_2Cl_2 of a) ligands **L1** (blue), **L2** (red), **L3** (violet), and **L4** (grey) and b) complexes **Cu1** (blue), **Cu2** (red), **Cu3** (violet), and **Cu4** (grey).

Energies of the molecular orbitals closer to the frontier region computed for all the ligands and complexes are listed in Table S9 along with the HOMO–LUMO energy gap, namely $\Delta_{H\text{-}L}$. The computed absorption spectra for **L1–L4** are in good agreement with experimental data (*cf.* Figure 3a and Figure 5a). For all proligands, a first transition is computed around 420 nm for **L1**, **L2** and **L3** and 440 nm for **L4** (Table S8), corresponding to their $S_0 \rightarrow S_1$ transition. According to the computed Electron Density Difference Maps (EDDMs), which are displayed

View Article Online
DOI: 10.1039/D6TC00899B

in Figure 6), this transition can be described as possessing singlet ^{1}LE (π–π^*) character on the benzimidazole (bim) and benzothiazole (btz) substituents with some ^{1}ICT from the TzTz toward the btz and bim. The features of the absorption profile observed experimentally can be attributed with confidence to the vibronic progression involving the rigid π-conjugated scaffold. A second significant transition appears at much higher energy, between 290 to 310 nm due to the $S_0 \rightarrow S_6$ transition which is mainly a ^{1}ICT from the btz to the TzTz core. No other transition being present in this energy range with significant absorbing intensity.

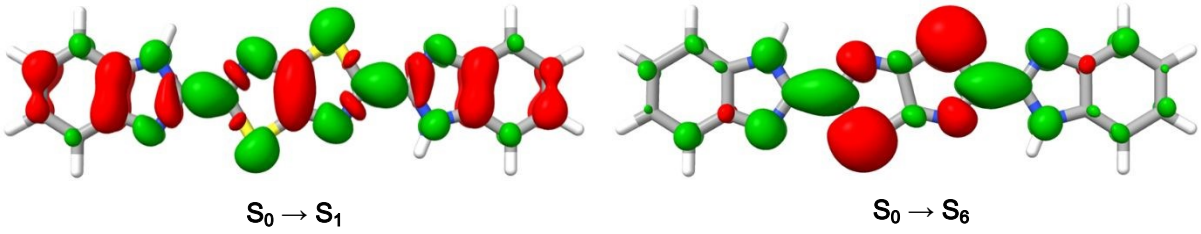

Figure 6. EDDMs between the ground and the excited state for S_1 (*left*) and S_6 (*right*) absorbing states of **L1**. Electronically depleted and enriched areas are shown in red and green colors, respectively.

As far as the complexes are concerned, the LUMO remains located on the TzTz ligand, whereas the HOMO and HOMO-1 are mainly located on the copper centers. The highest occupied orbital located on the ligand is the HOMO-2 for **Cu1**–**Cu3**, and HOMO-5 for **Cu4**. The computed absorption spectra nicely agree with the experimental ones (*cf.* Figure 3b and Figure 5b) and the list of computed transition are collected in Table S10 of the Supplementary Information. The spectra are similar for the four complexes and the THEODore analysis[45] of the computed states is detailed in Figure S26. The computed spectra present a first band above λ_{abs} = 500 nm corresponding to a set of charge transfer states either from the copper cation or from the disphosphine ligand towards the central TzTz ligand that can be overall described with admixed of ^{1}MLCT and ^{1}LLCT character. This corresponds to the band shoulder observed experimentally at λ_{abs} = 480–550 nm (Figure 3b). Moreover, a very intense band is calculated at λ_{abs} = *ca.* 445 nm which corresponds to states with an major contribution having large LC character located on the TzTz ligand, being similar for the four complexes. As an example, this transition involves S_5 and S_6 in **Cu1** and can be ascribed to a LC state slightly admixed with a MLCT manifold (Figure 7). On the other hand, the absorbing S_7 state possess an almost pure ^{1}LC character. These states are bathochromically shifted compared to the pure ligand due to perturbation of the coordinated metal centre expectantly. These peaks correspond to the intense experimental absorption observed at λ_{abs} = *ca.* 410 nm. In good agreement with experimental

data, the computed spectra do not present weak absorption process in the range λ_{abs} = 300–400 nm dominated by ^{1}LLCT transitions from the P^P from the TzTz ligand.

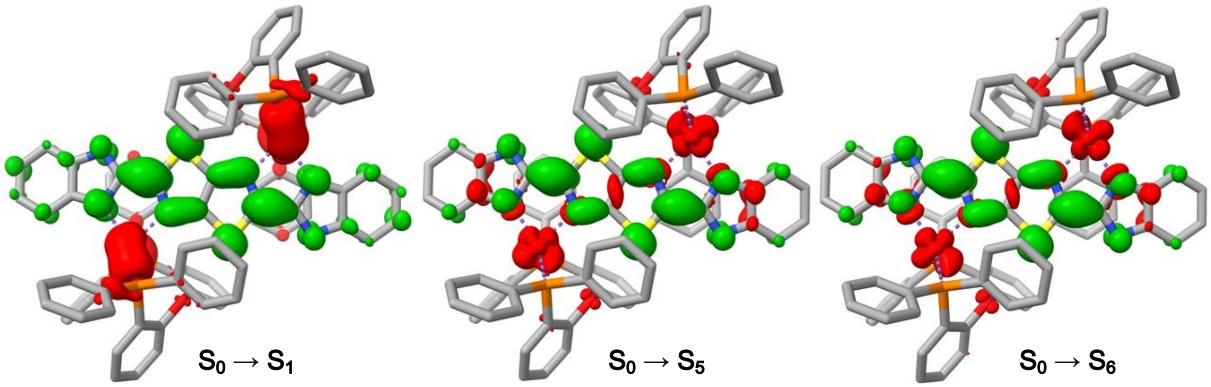

Figure 7. EDDMs between the ground and the excited state for S_1 (*left*), S_5 (*center*), and S_6 (*right*) absorbing states of **Cu1**. Electronically depleted and enriched areas are shown in red and green colors, respectively.

Electrochemical and Electroluminescent Properties of LECs

Based on their optical properties, complexes **Cu1** and **Cu4** were selected for further investigation and for the preparation of light emitting devices. Amongst the complexes of the series, the former resulted to be the most emissive one, whereas the latter displays the most bathochromically shifted emission spectra. The electrochemical properties of all the investigated complexes were assessed by means of cyclic voltammetry in CH_2Cl_2/0.1 M $TBAPF_6$ solution. The data are listed in Table 5.

Table 5. Electrochemical data recorded for the binuclear **Cu1** and **Cu4** complexes in CH_2Cl_2 / 0.1 M $TBAPF_6$ solution. Potential values are given against ferricenium/ferrocene (Fc^+|Fc) couple.

Complex	$E_{p,O_1,i}$ [V]	$E^0_{R_1,i}$ [V]	$E^0_{R_2,i}$ [V]	$e\Delta E_{H-L}$ [eV][c]
Cu1	+0.99[a]	-1.50[a]	-1.91[a]	~2.50
Cu4	+0.92[a]	-1.11[b]	-1.65[b]	~2.03

[a] Irreversible process. Only the peak potential, E_p, can be reported. [b] Reversible process, unless otherwise stated. The formal potential, E^0, was calculated as the average of the cathodic and anodic peak of the process. [c] The electrochemical band gap $e\Delta E_{H-L}$, was calculated as the difference between the peak potential of $O_{1,i}$ process and the peak potential or formal potential of $R_{1,i}$ process.

View Article Online
DOI: 10.1039/D6TC00899B

In the positive-going scan, **Cu1** and **Cu4** showed an irreversible oxidation process O_i (with i denoting the investigated compound), whose peak potentials E_p fall within the range +0.92 - +0.99 V vs Ferricenium/Ferrocene ($Fc^+|Fc^0$) redox couple, used as the internal standard. This redox process can be confidently ascribed to the oxidation that is mainly centered onto the metal. Moreover, once the potential scan is reverted a cathodic peak appeared in the range 0 – 0.5 V, which might be related to the reduction of the of species forming during the irreversible oxidation process, more likely followed by a chemical reaction (EC process), as previously observed for similar complexes.[23] Instead, in the negative-going scan, up to three reduction processes $R_{n,i}$ (where n denotes the process number and i the investigated compound) occurred, which are mainly irreversible for **Cu1** and reversible for **Cu4**, respectively. Therefore, peak potential and standard potential are provided, respectively, which fall within the range from –1.11 to –1.91 V vs $Fc^+|Fc^0$. Furthermore, the electrochemical energy band gap (e-$\Delta E_{H\text{-}L}$) for the HOMO-LUMO has been estimated from the O_1 and R_1 processes, taking into account the respective potential values for the irreversible and/or reversible processes. Overall, these findings agree well with the optical properties (see above) and support the idea that these complexes are potentially suitable candidates in the field of solid-state electroluminescence devices.

To investigate the EL characteristics of the proposed complexes, LEC devices were fabricated and characterized. Experimental details are described in the Supporting Information. For each complex, device performance was optimized by evaluating three emissive-layer thicknesses under the optimal bias condition (see device architecture and energy levels in Figure S5). The EL data of the fabricated LECs are summarized in Table 6. Time-dependent EL spectra of the LECs based on **Cu1** and **Cu4** with different thicknesses are presented in Figures S28a–c and S29a–c of the Supporting Information. Only minor spectral variations were observed during operation, indicating that microcavity effects arising from shifts of the emission zone during device operation[47,48] are negligible for relatively thin LECs (<200 nm). The stabilized EL spectra of LECs employing **Cu1** and **Cu4** with different emissive-layer thicknesses are shown in Figure 8a and 8b, respectively. **Cu1** exhibits deep-red EL emission ($\lambda_{em,max} \approx 700$ nm), whereas **Cu4** displays NIR EL emission ($\lambda_{em,max} \approx 770$ nm). In both cases, the EL spectra largely resemble the corresponding PL spectra, suggesting similar emission mechanisms.

The time-dependent current density, light output, and EQE of the LECs based on complexes **Cu1** and **Cu4** with different emissive-layer thicknesses are shown in Figure 9a–c

View Article Online
DOI: 10.1039/D6TC00899B

and Figure S30a–c of the ESI, respectively. All devices exhibit similar temporal evolutions of their EL characteristics. Upon bias application, mobile ions in the emissive layer drift toward the electrodes, gradually forming electrochemically doped regions that facilitate charge injection. Consequently, both the current density and light output rapidly increase at the initial stage of device operation. After reaching their maxima, the current density and light output progressively decrease, which is attributed to material degradation during prolonged operation. Meanwhile, the formation of doped layers improves carrier balance in the device, resulting in a rapid rise in EQE shortly after bias application, followed by a gradual decline due to the same degradation processes.

For the **Cu1**-based devices, the peak EQE increases with increasing emissive-layer thickness (Table 6). A thicker emissive layer enlarges the separation between the emission zone and the electrochemically doped regions, thereby suppressing exciton quenching.[49] In addition, device thickness influences the optical microcavity effect and thus the light-extraction efficiency, which also contributes to EQE optimization.[48] Owing to the limited solubility of **Cu1** in dichloromethane, further increases in emissive-layer thickness were not feasible. The thickest **Cu1**-based device (120 nm) therefore delivered the highest EQE of 0.49%.

In contrast, the better solubility of **Cu4** allowed the fabrication of thicker emissive layers. The optimized **Cu4**-based device with a thickness of 175 nm exhibited a maximum EQE of 0.09%. To date, only a limited number of NIR Cu(I) LECs with EL peak wavelengths exceeding 750 nm have been reported.[23,24] Compared with those, the **Cu4**-based devices show comparable EL peak wavelengths and peak EQEs. Notably, they exhibit a smaller thickness-dependent EL spectral shift arising from the microcavity effect, resulting in improved spectral stability.

The carrier balance in LECs based on complexes **Cu1** and **Cu4** may be influenced by the ligand environment of the complexes. To evaluate this effect, the EQE of the devices was analyzed using Equation 3, which describes the key factors governing the EQE of LECs:

$$\eta_{EQE} = \eta_{out} \times \gamma \times \eta_{S,T} \times \eta_{QY} \quad \text{(eqn. 3)}$$

In this equation, η_{EQE} represents the measured device EQE, η_{out} the optical outcoupling efficiency, γ the carrier-balance factor, $\eta_{S,T}$ the efficiency of emissive exciton formation, and η_{QY} the solid-state PLQY of the emitter. For phosphorescent complexes, both singlet and triplet

View Article Online
DOI: 10.1039/D0TC00899B

excitons can be effectively utilized, giving $\eta_{S,T}$ = 100%. The optical outcoupling efficiency of LECs is typically estimated to be approximately 20–30%.[48]

Using the measured EQEs (Table 6) and solid-state PLQYs (Table 4), and assuming η_{out} = 25%, the carrier-balance factors (γ) were estimated to be 49% and 36% for the **Cu1**- and **Cu4**-based LECs, respectively. Although uncertainties may arise from the estimation of η_{out}, the calculated γ values suggest that the benzimidazole ligand in **Cu1** provides slightly improved carrier balance compared with the benzothiazole ligand in **Cu4**.

Table 6. Summary of the EL characteristics of the LECs based on complex **Cu1** or **Cu4** (80 wt.%) and [$BMIM^+(PF_6)^-$] (20 wt.%).

Complex	Concentration (mg mL^{-1})[a]	Spin speed (rpm)[b]	Thickness (nm)	Bias (V)	EL_{max} (nm)[c]	L_{max} (μW cm^{-2})[d]	$\eta_{ext,\,max}$ (%)[e]	$\eta_{P,\,max}$ (mW W^{-1})[f]
	30	2000	71	2.3	686	2.91	0.22	1.70
Cu1	30	1000	111	2.3	694	3.65	0.40	3.00
	30	750	120	2.4	697	3.22	0.49	3.69
	50	2000	144	2.5	772	0.36	0.085	0.53
Cu4	60	2000	175	3	773	0.76	0.090	0.46
	70	2000	213	2.5	776	0.21	0.063	0.39

[a] Solution concentration for spin coating. [b] Spin speed for spin coating. [c] Stabilized EL emission peak wavelength. [d] Maximal light output power. [e] Maximal external quantum efficiency.[f] Maximal power efficiency.

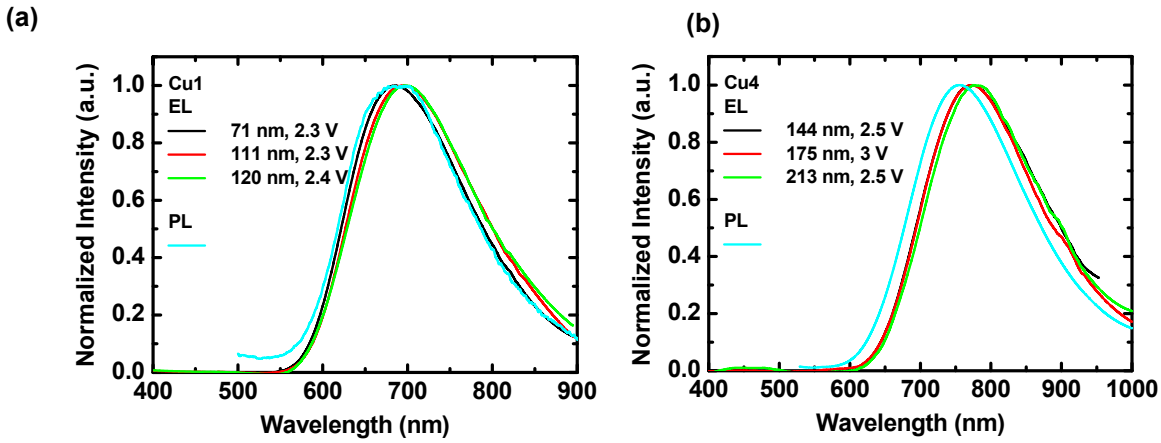

Figure 8. Stabilized EL spectra of LECs based on (a) **Cu1** and (b) **Cu4** with different emissive-layer thicknesses. The PL spectra are included for comparison.

View Article Online
DOI: 10.1039/D6TC00899B

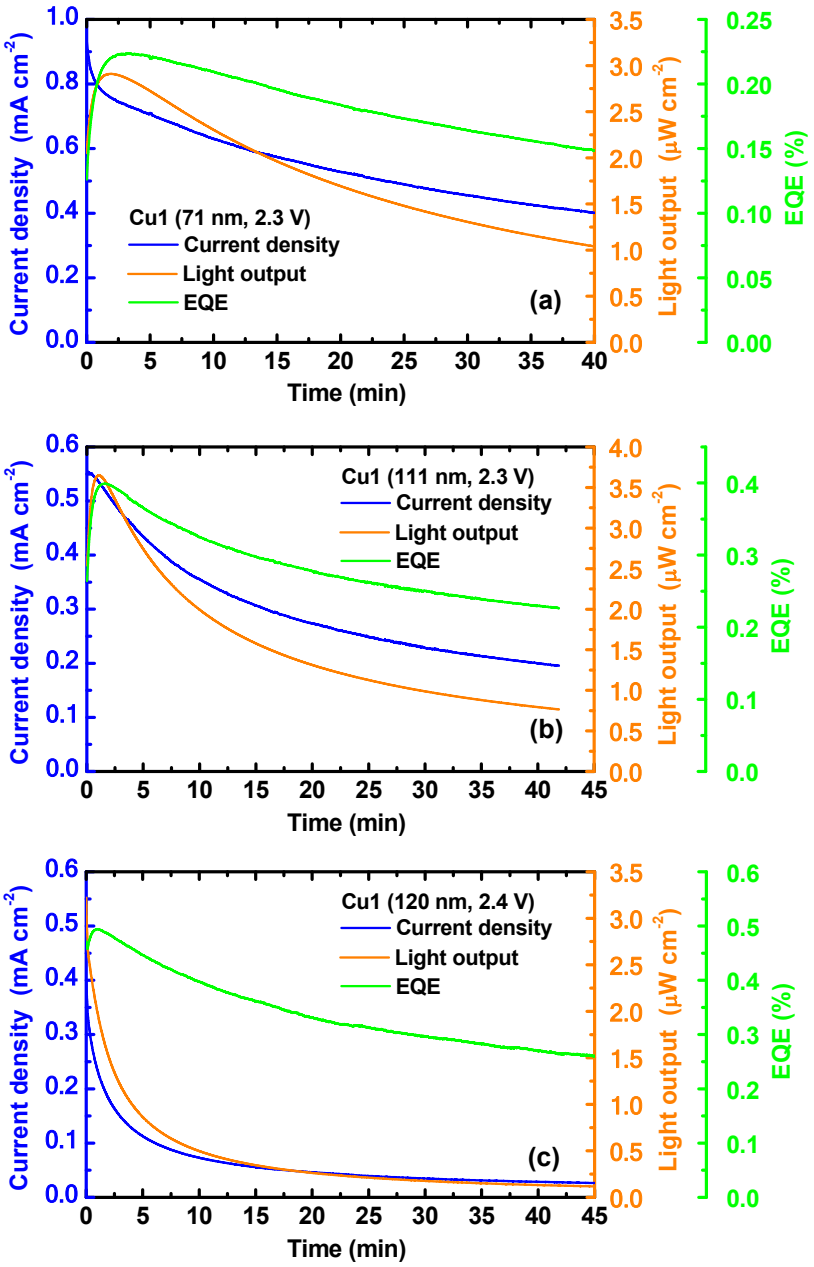

Figure 9. Time-dependent current density, light output, and EQE of LECs based on **Cu1** with emissive-layer thicknesses of (a) 71, (b) 111, and (c) 120 nm. The applied bias voltage is indicated in each panel.

Conclusion

A small family of four new binuclear Cu(I) complexes of general structure $[Cu^{I}_2(N^N–N^N)(DPEphos)_2]^{2+}$ where N^N–N^N is a *bis*-bidentate benzimidazolyl- or benzothiazolyl-functionalized thiazolo[4,5-*d*]thiazole ligand, was herein presented. The four complexes all displayed photoluminescence in dilute degassed and air-equilibrated CH_2Cl_2 in the deep-red to

View Article Online
DOI: 10.1039/D6TC00899B

NIR region of the visible spectrum, with complexes **Cu2** and **Cu3** reaching $\lambda_{em,max}$ as high as 775 nm and PLQY as high as 0.55%, leading to a %NIR ratio of around 50%. Comparing these values with those of NIR emitters previously reported by our group such as Cu(I) complexes **Cu-D3**[24] ($\lambda_{em,max}$ = 790 nm and PLQY 0.04% in degassed CH_2Cl_2), it can be seen how indeed the addition of further heteroatoms can cause a bathochromic shift in the emission, albeit π-extension of the system still plays an important role. Despite their overall low PLQY values in solution and the hypsochromic shift that generally accompanies solid-state measurements, powder samples displayed $\lambda_{em,max}$ as high as 757 nm (**Cu4**) and PLQY values as high as 4% (**Cu1**). The interesting deep-red to NIR emission displayed by these complexes prompted their use as electroactive materials in LEC devices. Remarkably, complex **Cu4** displayed NIR electroluminescence with maxima λ_{EL} above 770 nm and improved spectral stability compared to other electroactive Cu(I) complexes emitting in the same spectral region and previously reported in the literature and device performances comparable to NIR emitters based on noble metals. Overall, these results confirm that dinuclear Cu(I) complexes may act as valuable alternative to NIR-emitting Ir(III) and Pt(II) phosphors.

Experimental Section

CCDC 2402732 (**L3**), 2402730 (**Cu1**), 2402731 (**Cu2**), 2402732 (**Cu3**), 2412038 (**Cu4**) contains the supplementary crystallographic data for this paper. These data can be obtained free of charge from The Cambridge Crystallographic Data Centre via http://www.ccdc.cam.ac.uk/data_request/cif .

Acknowledgements

M.M. gratefully acknowledges the Université de Strasbourg and CNRS for financial support, and the French Agence Nationale de Recherche (ANR) for funding the grants ANR-22-CE07-0049-02 “BoostOLED”, ANR-23-CE29-0019 “QUINOC”, and ANR-24-CE29-2108 “E-Polar”. V.G. gratefully acknowledges the Collège Doctoral of the Université de Strasbourg for co-funding his PhD fellowship. N. Gruber and C. Bailly of the Service de Radiocristallographie, Fédération de Chimie Le Bel – UAR2042, Université de Strasbourg & CNRS are kindly acknowledged for the help in solving the X-ray structures. C.G. thanks the HPC of Strasbourg for computational time. This work was supported by the Higher Education

View Article Online
DOI: 10.1039/D6TC00899B

Sprout Project of the National Yang Ming Chiao Tung University and Ministry of Education (MOE), Taiwan.

References

1 G. Qian and Z. Y. Wang, *Chem. Asian J.*, 2010, **5**, 1006–1029.

2 Q. Pei, G. Yu, C. Zhang, Y. Yang and A. J. Heeger, *Science*, 1995, **269**, 1086–1088.

3 Y.-D. Lin, C.-W. Lu and H.-C. Su, *Chem. Eur. J.*, 2023, **29**, e202202985.

4 A. Pertegás, D. Tordera, J. J. Serrano-Pérez, E. Ortí and H. J. Bolink, *J. Am. Chem. Soc.*, 2013, **135**, 18008–18011.

5 M. Mone, S. Tang, Z. Genene, P. Murto, M. Jevric, X. Zou, J. Ràfols-Ribé, B. A. Abdulahi, J. Wang, W. Mammo, M. R. Andersson, L. Edman and E. Wang, *Adv. Optical Mater.*, 2021, **9**, 2001701.

6 Y. Chen, Y.-X. Wang, C.-W. Lu and H.-C. Su, *J. Mater. Chem. C*, 2022, **10**, 11211–11219.

7 W. Xiong, S. Tang, P. Murto, W. Zhu, L. Edman and E. Wang, *Adv. Optical Mater.*, 2019, **7**, 1900280.

8 S. Tang, P. Murto, J. Wang, C. Larsen, M. R. Andersson, E. Wang and L. Edman, *Adv. Opt. Mater.*, 2019, **7**, 1900451.

9 S. Xun, J. Zhang, X. Li, D. Ma and Z. Y. Wang, *Synth. Met.*, 2008, **158**, 484–488.

10 P.-C. Huang, G. Krucaite, H.-C. Su and S. Grigalevicius, *Phys. Chem. Chem. Phys.*, 2015, **17**, 17253–17259.

11 B. N. Bideh, C. Roldán-Carmona, H. Shahroosvand and M. K. Nazeeruddin, *J. Mater. Chem. C*, 2016, **4**, 9674–9679.

12 A. K. Pal, D. B. Cordes, A. M. Z. Slawin, C. Momblona, A. Pertegás, E. Ortí, H. J. Bolink and E. Zysman-Colman, *RSC Adv.*, 2017, **7**, 31833–31837.

13 Y.-H. Su, Y.-C. Ji, Y.-T. Huang, D. Luo, S.-W. Liu, Z.-P. Yang, C.-W. Lu, C.-H. Chang and H.-C. Su, *J. Mater. Chem. C*, 2022, **10**, 18137–18146.

14 B. Pashaei, H. Shahroosvand, H. Douroudgari, S. Abaspour, M. Vahedpour and M. K. Nazeeruddin, *Inorg. Chem.*, 2023, **62**, 7622–7635.

15 B. Pashaei, H. Shahroosvand, M. Moharramnezhad, M. A. Kamyabi, H. Bakhshi, M. Pilkington and M. K. Nazeeruddin, *Inorg. Chem.*, 2021, **60**, 17040–17050.

16 Y.-D. Lin, P.-W. Hsiao, W.-Y. Chen, S.-Y. Wu, W.-M. Zhang, C.-W. Lu and H.-C. Su, *Chem. Eng. J.*, 2023, **469**, 144055.

17 J. E. Namanga, N. Gerlitzki, B. Mallick and A.-V. Mudring, *J. Mater. Chem. C*, 2017, **5**,

View Article Online
DOI: 10.1039/D6TC00899B

3049–3055.

18 E. C. Constable, C. E. Housecroft, G. E. Schneider, J. A. Zampese, H. J. Bolink, A. Pertegás and C. Roldan-Carmona, *Dalton Trans.*, 2014, **43**, 4653–4667.

19 G.-Y. Chen, B.-R. Chang, T.-A. Shih, C.-H. Lin, C.-L. Lo, Y.-Z. Chen, Y.-X. Liu, Y.-R. Li, J.-T. Guo, C.-W. Lu, Z.-P. Yang and H.-C. Su, *Chem. Eur. J.*, 2019, **25**, 5489–5497.

20 A. R. Hosseini, C. Y. Koh, J. D. Slinker, S. Flores-Torres, H. D. Abruña and G. G. Malliaras, *Chem. Mater.*, 2005, **17**, 6114–6116.

21 L. M. Cinninger, L. D. Bastatas, Y. Shen, B. J. Holliday and J. D. Slinker, *Dalton Trans.*, 2019, **48**, 9684–9691.

22 S. Lipinski, L. M. Cavinato, T. Pickl, G. Biffi, A. Pöthig, P. B. Coto, J. Fernández-Cestau and R. D. Costa, *Adv. Optical Mater.*, 2023, **11**, 2203145.

23 A. Jouaiti, L. Ballerini, H. Shen, R. Viel, F. Polo, N. Kyritsakas, S. Haacke, Y. Huang, C. Lu, C. Gourlaouen, H. Su and M. Mauro, *Angew. Chem. Int. Ed.*, 2023, **62**, e202305569.

24 A. Jouaiti, L. Ballerini, W.-M. Zhang, F. Polo, C. Gourlaouen, H.-C. Su and M. Mauro, *Adv. Optical Mater.*, 2025, **13**, 2402666.

25 H. Yersin and K. L. Bray, eds., *Transition metal and rare earth compounds: excited states, transitions, interactions I*, Springer, Berlin, Heidelberg, 2001.

26 R. Englman and J. Jortner, *Mol. Phys.*, 1970, **18**, 145–164.

27 J. V. Caspar and T. J. Meyer, *J. Phys. Chem.*, 1983, **87**, 952–957.

28 V. Balzani and S. Campagna, *Photochemistry and photophysics of coordination compounds*, Springer, Berlin, 2007.

29 D. G. Cuttell, S.-M. Kuang, P. E. Fanwick, D. R. McMillin and R. A. Walton, *J. Am. Chem. Soc.*, 2002, **124**, 6–7.

30 B. Hupp, C. Schiller, C. Lenczyk, M. Stanoppi, K. Edkins, A. Lorbach and A. Steffen, *Inorg. Chem.*, 2017, **56**, 8996–9008.

31 E. Fresta, M. D. Weber, J. Fernandez-Cestau and R. D. Costa, *Adv. Optical Mater.*, 2019, **7**, 1900830.

32 D. Bevk, L. Marin, L. Lutsen, D. Vanderzande and W. Maes, *RSC Adv.*, 2013, **3**, 11418.

33 A. Dessì, M. Calamante, A. Mordini, L. Zani, M. Taddei and G. Reginato, *RSC Adv.*, 2013, **4**, 1322–1328.

34 E. Fresta, J. M. Carbonell-Vilar, J. Yu, D. Armentano, J. Cano, M. Viciano-Chumillas and R. D. Costa, *Adv. Funct. Mater.*, 2019, **29**, 1901797.

35 V. Giuso, J.-Y.Zhuang, C. Gourlaouen, C. Cebrián, H..-C. Su, M. Mauro, *manuscript submitted*.

View Article Online
DOI: 10.1039/D6TC00899B

36 V. Giuso, C. Gourlaouen, L. Arrico, L. Di Bari, M. Mauro, *manuscript submitted*.

37 K. F. Baranova, A. A. Titov, A. F. Smol'yakov, A. Y. Chernyadyev, O. A. Filippov and E. S. Shubina, *Molecules*, 2021, **26**, 6869.

38 L. Yang, D. R. Powell and R. P. Houser, *Dalton Trans.*, 2007, 955–964.

39 A. Okuniewski, D. Rosiak, J. Chojnacki and B. Becker, *Polyhedron*, 2015, **90**, 47–57.

40 V. Giuso, C. Gourlaouen, C. Cebrián, A. Jouaiti, M. Mauro, *manuscript in preparation*.

41 International Commission on Illumination, CIE 17-21-004.

42 R. Czerwieniec, M. J. Leitl, H. H. H. Homeier and H. Yersin, *Coord. Chem. Rev.*, 2016, **325**, 2–28.

43 J. Brooks, Y. Babayan, S. Lamansky, P. I. Djurovich, I. Tsyba, R. Bau and M. E. Thompson, *Inorg. Chem.*, 2002, **41**, 3055–3066.

44 C. D. Ertl, C. Momblona, A. Pertegás, J. M. Junquera-Hernández, M.-G. La-Placa, A. Prescimone, E. Ortí, C. E. Housecroft, E. C. Constable and H. J. Bolink, *J. Am. Chem. Soc.*, 2017, **139**, 3237–3248.

45 L. Ballerini, W.-M. Zhang, T. Groizard, C. Gourlaouen, F. Polo, A. Jouaiti, H.-C. Su and M. Mauro, *J. Mater. Chem. C*, 2024, **12**, 12769–12783.

46 F. Plasser, *J. Chem. Phys.*, 2020, **152**, 084108.

47 H.-C. Su, *ChemPlusChem*, 2018, **83**, 197–210.

48 R.-H. Yi, C.-L. Lo, D. Luo, C.-H. Lin, S.-W. Weng, C.-W. Lu, S.-W. Liu, C.-H. Chang and H.-C. Su, *ACS Appl. Mater. Interfaces*, 2020, **12**, 14254–14264.

49 J.-S. Lu, J.-C. Kuo and H.-C. Su, *Org. Electron.*, 2013, **14**, 3379–3384.

View Article Online
DOI: 10.1039/D6TC00899B

Data Availability Statement

Detailed synthetic procedures, NMR and HR-ESI-MS data, crystallographic structures, additional absorption and emission data, additional computational data and Electroluminescence performances (PDF).

CCDC 2402732 (**L3**), 2402730 (**Cu1**), 2402731 (**Cu2**), 2402732 (**Cu3**), 2412038 (**Cu4**) contains the supplementary crystallographic data for this paper. These data can be obtained free of charge from The Cambridge Crystallographic Data Centre via http://www.ccdc.cam.ac.uk/data_request/cif .